Eur. Phys. J. Plus (2021) 136:1104
https://doi.org/10.1140/epjp/s13360-021-02060-0

THE EUROPEAN PHYSICAL JOURNAL PLUS

Regular Article

Ion–electron energy transfer in kinetic and fluid modelling of the tokamak scrape-off layer

D Power[1,a], **S Mijin**[2], **F Militello**[2], **R J Kingham**[1]

[1] Blackett Lab., Plasma Physics Group, Imperial College London, London SW7 2AZ, UK
[2] CCFE, Culham Science Centre, Abingdon, Oxon OX14 3BD, UK

Received: 5 January 2021 / Accepted: 11 October 2021

Abstract Using the 1D kinetic electron code SOL-KiT, simulations of the divertor tokamak scrape-off layer were carried out to explore the presence of kinetic effects in energy transfer between the ions and electrons. During steady-state conditions, it was found that the ion–electron energy transfer is well described by a fluid model, with only minimal differences seen when electrons are treated kinetically. During transient regimes (featuring a burst of energy into the scrape-off layer), we see evidence of enhanced energy exchange when calculated kinetically as compared to a fluid model. The kinetic correction represents an additional 8–55% ion–electron energy transfer across the domain, depending on the pre-transient plasma collisionality. Compared to the total energy going into the plasma during the transient, the correction is less than 1%, so its impact on plasma profiles may be small. The effect is seen to increase in strength along the domain, peaking in front of the divertor target. The overall discrepancy (integrated along the domain) increases during the transient energy burst and disappears on a similar timescale. However, at the target the effect peaks later and takes several multiples of the transient duration to relax. This effect may be only partially explained by an additional population of cold electrons arising from neutral ionization.

1 Introduction

In magnetically confined fusion devices such as tokamaks, the region of plasma between the reactor walls and the core plasma helps to define its performance. This region, characterized by open magnetic field lines culminating at solid targets, is called the scrape-off layer (SOL). In a divertor tokamak, particles and energy make their way from the core to the reactor walls via the SOL. Transport occurs both along and across the field lines, but the strong magnetic fields ensure parallel transport dominates over perpendicular transport. For present and future reactors, quantifying this parallel transport is important in predicting effects such as the qualitative behaviour of the SOL, heat loads to the reactor walls and the sputtering yield of impurities from solid surfaces into the plasma.

Treatment of parallel transport in the SOL is often done using fluid models [1–3], developed in a similar manner to the fluid closure of Braginskii [4]. However, fluid models fail to account for some experimental observations such as the electron temperature at the solid targets [5]. This may be explained due to 'kinetic effects', defined broadly as anything result-

[a] e-mail: d.power19@imperial.ac.uk (corresponding author)

Published online: 02 November 2021

ing from deviations from a velocity distribution of the plasma particles which is close to Maxwellian. Such effects in plasmas may arise due to steep temperature gradients, plasma–surface interactions or due to atomic and molecular processes. Each of these is present in the edge plasma in a divertor tokamak, a tokamak configuration designed to distance the plasma–wall interface from the core plasma. Steep temperature gradients in particular are a feature of the 'detached' divertor SOL, a favourable operating regime featuring a neutral cloud between the plasma-facing components and the hot upstream plasma.

Because of differences in the ability of ions and electrons to conduct heat along and out of the SOL, we expect the ions to generally reach higher temperatures in the SOL if the total power going into each species via cross-field transport from the core is approximately equal. Therefore, energy is expected to flow to the electrons through elastic ion–electron collisions. This additional source/sink term for each species may play a role in determining plasma behaviour in the SOL and the eventual escape mechanism for energy that makes its way into the SOL. For example, physical sputtering yields are determined primarily by the amount of heat flux carried to the solid surfaces by the ions, while the amount of energy radiated away via inelastic collisions with neutral particles depends more on the properties of the electrons. Since there is evidence of kinetic effects in other aspects of SOL plasma behaviour, it is natural to investigate whether a fluid model is adequate to describe ion–electron energy exchange. To the authors' knowledge, such a study has not been carried out previously.

Here, results are presented of 1D simulations of the divertor SOL using the kinetic electron code SOL-KiT [6], which is outlined in Sect. 2.1. While such 1D studies might lack precise quantitative predictive power, they are useful for understanding qualitative edge plasma behaviour, which is the purpose of this study. The SOL-KiT model has been extended to include a fluid ion temperature equation, allowing the electron and ion temperatures to decouple. Large differences in temperature are expected outside of highly collisional regimes due to differences in their parallel heat conductivity. The extensions to the SOL-KiT model are discussed in Sect. 2.2. Simulations of equilibria and transients have been run for a divertor SOL in a medium-sized tokamak at a range of different collisionalities, described in Sect. 3. Focus is given to the transfer of energy between electrons and ions, and it will be shown (Sect. 4) that a kinetic treatment of the electrons can result in deviations of the amount of energy transfer as compared to a fluid approximation. Potential causes and consequences of this effect will be discussed in Sect. 5.

2 Physical model

SOL-KiT is a fully implicit 1D plasma code [6] which has been used to study kinetic effects in parallel electron transport in the divertor SOL [7]. We will briefly outline the physical model implemented in SOL-KiT, followed by the extensions to the ion model which have facilitated the analysis presented here.

2.1 SOL-KiT

SOL-KiT models a hydrogenic plasma consisting of electrons, which may be treated either as a fluid or kinetically, fluid ions and diffusive neutral atoms (including a collisional radiative model for neutral excited states). The primary aim of SOL-KiT is to provide a consistent means of comparing a fluid plasma model with a model featuring kinetic electrons. As such, an important feature of SOL-KiT is that it can recover the classical transport coefficients in highly collisional plasmas, including the Spitzer–Härm heat flow, while demonstrating

non-local effects in low-collisionality domains. This has been shown in [6,7]. The implicit numerical scheme used by SOL-KiT also ensures that fast phenomena on the timescale of the plasma oscillation period are effectively smoothed out when using comparatively large timesteps.

Here, we will briefly outline the SOL-KiT code; the interested reader is referred to [6] for a more detailed explanation of the model, numerics and benchmarking.

2.1.1 Fluid model

The fluid model for electrons consists of equations for the density n_e,

$$\frac{\partial n_e}{\partial t} + \frac{\partial \left(n_e u_e\right)}{\partial x} = S, \tag{1}$$

flow velocity u_e,

$$\frac{\partial u_e}{\partial t} = -u_e \frac{\partial u_e}{\partial x} - \frac{e}{m_e} E + \frac{R_e}{m_e n_e} - \frac{S}{n_e} u_e - \frac{1}{m_e n_e} \frac{\partial \left(n_e k T_e\right)}{\partial x} \tag{2}$$

and temperature T_e,

$$\frac{\partial k T_e}{\partial t} = -u_e \frac{\partial k T_e}{\partial x} + \frac{2}{3}\left[\frac{Q_e}{n_e} - k T_e \frac{\partial u_e}{\partial x} - \frac{1}{n_e}\frac{\partial q_e}{\partial x} - \frac{S}{n_e}\left(\frac{3}{2} k T_e - \frac{m_e u_e^2}{2}\right) - \frac{u_e R_e}{n_e}\right]. \tag{3}$$

The spatial domain is along the x-axis. The parallel electric field is given by E. The constants e, m_e and k are the elementary electron charge, electron mass and Boltzmann's constant, respectively. S, R_e and Q_e are sources of particles (from ionization and recombination), friction (from electron–ion and electron–neutral collisions) and heat (from electron–ion and electron–neutral collisions as well as external heating). Electron–neutral processes, and the associated transfer of particles, momentum and energy, are described in Sect. 2.1.2. The Braginskii form is used for the electron–ion contribution to R_e [4], $R_{ei} = -\frac{m_e n_e}{\tau_e} 0.51\left(u_e - u_i\right) - 0.71 n_e \frac{\partial (k T_e)}{\partial x}$. Closure of these fluid equations is achieved with the Braginskii expression for heat flow [4], $q_e = -\kappa_e \frac{\partial (k T_e)}{\partial x} + 0.71 n_e k T_e \left(u_e - u_i\right)$, with the Spitzer–Härm value for heat conductivity κ_e [8].

The ion density, n_i, is not modelled directly; instead quasi-neutrality is enforced via $Z n_i = n_e$, where the ion charge is Ze. The ion flow velocity, u_i, is evolved using a very similar equation to (2) featuring the ion mass, m_i,

$$\frac{\partial u_i}{\partial t} = -u_i \frac{\partial u_i}{\partial x} + \frac{Ze}{m_i} E + \frac{R_i}{m_i n_i} - \frac{S}{n_i} u_i - \frac{1}{m_i n_i} \frac{\partial \left(n_i k T_i\right)}{\partial x}. \tag{4}$$

Particle sources S are the same for both species. R_i has contributions from ion–electron friction (obtained by enforcing overall momentum conservation, $R_{ie} = -R_{ei}$) and ion–neutral friction via charge exchange collisions, R_{CX}. A simplified form of charge exchange is considered, where neutrals are effectively considered as a stationary target, so that $R_{CX} = -n_i m_i u_i |u_i| n_n \sigma_{CX}$. The neutral densities and charge exchange cross sections are summed over all tracked excited states, with cross-section data obtained from Janev [9].

The electric field is calculated using Ampère–Maxwell's law, containing only the displacement current,

$$\frac{\partial E}{\partial t} = -\frac{1}{\varepsilon_0}(j_e + j_i). \tag{5}$$

The electron and ion currents are calculated in the fluid model as $j_{i,e} = q_{i,e} n_{i,e} u_{i,e}$, where $q_i = Ze$ and $q_e = -e$, and ε_0 is the vacuum permittivity.

Atomic neutrals are treated with a diffusive model, where the density of each excited state b is tracked using Fick's law for diffusion and a collisional radiative model (CRM) for the sources,

$$\frac{\partial n_b}{\partial t} = \frac{\partial}{\partial x}\left(D_b \frac{\partial n_b}{\partial x}\right) + S_b. \tag{6}$$

For a given state b, the source term S_b contains contributions from electron-impact excitation and ionization, spontaneous and collisional de-excitation, and radiative and three-body recombination. The 1D diffusion coefficient D_b is calculated using the charge exchange collision frequency.

2.1.2 Kinetic electron model

When the electrons are modelled kinetically, the electron velocity distribution function $f(x, \boldsymbol{v}, t)$ is evolved according to the 1D Vlasov–Fokker–Planck–Boltzmann (VFPB) equation,

$$\frac{\partial f(x, \boldsymbol{v}, t)}{\partial t} + v_x \frac{\partial f(x, \boldsymbol{v}, t)}{\partial x} - \frac{e}{m_e} E \frac{\partial f(x, \boldsymbol{v}, t)}{\partial v_x} = \sum_\alpha C_{e\text{-}\alpha}, \tag{7}$$

where $\boldsymbol{v}$ is the velocity space coordinate and $C_{e\text{-}\alpha}$ is the collision operator for collisions between electrons and species α (electrons, ions or neutral atoms). For collisions between charged particles (electron–electron and electron–ion), the Fokker–Planck collision operator is implemented. For collisions between electrons and neutral atoms, the Boltzmann collision integral is used.

Similar to codes such as IMPACT [10] and OSHUN [11], a spherical harmonic expansion of f is employed as a physically meaningful method of dimensionality reduction (described in detail in [12]). The Cartesian velocity coordinates (v_x, v_y, v_z) are expressed in spherical coordinates (v, θ, φ). Spherical harmonics allow us to write a function in this coordinate system as a product of associated Legendre polynomials, $P_l^m(\cos\theta)$, and the complex phase, $e^{im\varphi}$. The distribution function becomes

$$f(v, \theta, \varphi) = \sum_{l=0}^{\infty} \sum_{m=-l}^{l} f_l^m(v) P_l^{|m|}(\cos\theta) e^{im\varphi}.$$

Since the model is 1D and azimuthal symmetry about the x-axis is assumed, magnetic field effects are ignored and $m = 0$ always, reducing the decomposition to Legendre polynomials only (the m superscript is hereby dropped).

Transport quantities become natural functions of different harmonics of f in this formalism. For a scalar function in v, its moment uses the $l = 0$ harmonic,

$$\int \phi f(\boldsymbol{v}) d\boldsymbol{v} = 4\pi \int_0^\infty \phi f_0(v) v^2 dv.$$

Values for n_e and T_e can be obtained for $\phi = 1$ and $\phi = \frac{1}{2} m_e v^2$, respectively. If $\boldsymbol{a}$ is a vector function of v, its moment uses the $l = 1$ harmonic,

$$\int \boldsymbol{a} f(\boldsymbol{v}) d\boldsymbol{v} = \frac{4\pi}{3} \int_0^\infty \|a\| f_1 v^2 dv.$$

For $\boldsymbol{a} = -e\boldsymbol{v}$, we can obtain the electron current density, and $\boldsymbol{a} = \frac{1}{2} m_e v^2 \boldsymbol{v}$ gives the total energy flux. This can be continued for higher-order tensor quantities.

This process allows us to express the kinetic Eq. (7) as a series of equations in $f_l(x, v, t)$, up to some l_{max} for the highest resolved harmonic. The Fokker–Planck and Boltzmann collision operators are similarly decomposed according to the process outlined in [12]. Taking moments of the density, momentum and energy of the distribution function also allows direct comparison with the fluid electron model outlined in the previous section, enabling studies which seek to isolate kinetic effects, as well as for interfacing with the fluid ion and neutral model.

The particle source S, used in the fluid model for ions and electrons, is calculated through considering electron-impact ionization, radiative recombination and three-body recombination events. Ionization rates are calculated by taking moments of f_0. For ionizations from a given neutral state b, $K_b^{ion} = 4\pi \int dv v^3 f_0(v) \sigma_b^{ion}$, where σ_b^{ion} is the total ionization cross section, so that $S_{ion} = \sum_b K_b^{ion} n_b$. Excitation/deexcitation collisions are treated similarly, which contributes to the particle source S_b for the individual neutral states in (6). This same approach is taken when the fluid model for electrons is used, and f_0 is taken to be Maxwellian at the correct density and temperature. Three-body recombination is the inverse process to ionization and is treated via the principal of detailed balance [13,14], while Maxwellian radiative recombination rates are used, taken from [9].

A similar approach is taken for electron–ion and electron–neutral friction, R_{ei} and R_{en}, where the momentum moment of the relevant collision operators are taken. Because these are vector quantities, f_1 is required. For fluid electrons, $f_1(v) = -u_e \partial f_0 / \partial v$ with Maxwellian f_0. Finally, the electron–neutral energy exchange, Q_{en} can be calculated by taking the product of rate coefficients (calculated as described above) with the neutral density and the transition energy for a given process, summed over all neutral states and all processes considered. For a process which takes neutrals from state b to b' then,

$$Q_{en} = -\sum_{bb'} K_{b\to b'} n_b \varepsilon_{b\to b'},$$

where $\varepsilon_{b\to b'}$ is the transition energy of a given process. In this way, plasma cooling due to ionization, for example, is accounted for consistently across the fluid and kinetic model.

With kinetic electrons, the electric field (5) is solved by taking the current density moment of the electron distribution.

2.2 Extensions to the SOL-KiT model

In order to allow the ion and electron temperatures to decouple, an ion temperature equation has been added to SOL-KiT. This is analogous to the fluid electron temperature Eq. (3) and is developed in the same manner by taking moments of the kinetic equation and separating velocity into mean and random components [4]. The form implemented is

$$\frac{\partial kT_i}{\partial t} = -u_i \frac{\partial kT_i}{\partial x} + \frac{2}{3}\left[\frac{Q_i}{n_i} - kT_i \frac{\partial u_i}{\partial x} - \frac{1}{n_i}\frac{\partial q_i}{\partial x} - \frac{S}{n_i}\left(\frac{3}{2}kT_i - \frac{1}{2}m_i u_i^2\right) - \frac{u_i}{n_i}R_i\right]. \quad (8)$$

The friction term R_i and particle source S are the same as that used in the fluid model (see Sect. 2.1.1). The Braginskii form of the ion heat flow is used with Spitzer–Härm heat conductivity [4,8],

$$q_i = -\kappa_i \frac{\partial (kT_i)}{\partial x},$$

where $\kappa_i = 3.906 n_i k T_i \tau_i / m_i$, the ion collision time is

$$\tau_i = \frac{3\sqrt{m_i}(kT_i)^{\frac{3}{2}}(4\pi\epsilon_0)^2}{4\sqrt{\pi}Z^4 n_i \ln\Lambda e^4},$$

and $\ln\Lambda$ is the Coulomb logarithm.

Ion heating $Q_i = Q_{ext,i} + Q_{ie}$ arises from external heating (simulating input power to the SOL from the core plasma) and from collisions with electrons. For a given heat flux W_i entering over a heating length L_h, $Q_{ext,i} = W_i / L_h$. The electron–ion heat exchange is treated differently for fluid or kinetic electrons. For fluid electrons, a standard form [15] is used,

$$Q_{ie} = -Q_{ei} = -\frac{3m_e}{m_i}\frac{n_e k}{\tau_e}(T_i - T_e), \tag{9}$$

where the electron collision time is

$$\tau_e = \frac{3\sqrt{m_e}(kT_e)^{3/2}(4\pi\epsilon_0)^2}{4\sqrt{2\pi}Zn_e \ln\Lambda e^4}.$$

Note that a positive value of Q_{ei} here corresponds to energy moving from the ions to the electrons.

When electrons are considered kinetically, the energy moment is taken of the collision operator for electron–ion collisions, $C_{e\text{-}i}$, such that

$$Q_{ei} = \int d\boldsymbol{v}\frac{1}{2}m_e v^2 C_{e\text{-}i} = 4\pi\int dv\frac{1}{2}m_e v^4 C^0_{e\text{-}i}, \tag{10}$$

where the collision operator for f_0 is used, $C^0_{e\text{-}i}$, since Q_{ei} is a scalar quantity. $C^0_{e\text{-}i}$ is a function of both f_0 and F_0, the isotropic part of the ion distribution function. As described in [12], we obtain a form of this collision operator by reformulating the Rosenbluth potentials of the Fokker–Planck collision operator in terms of integral functions of the scattering species (in this case, ions) and, assuming a Maxwellian F_0, we arrive at

$$C^0_{e\text{-}i} = \frac{1}{v^2}\frac{\partial}{\partial v}\left[\frac{\Gamma_{ei} I^0_0 m_e}{m_i}\left(f_0 + \frac{kT_i}{m_e v}\frac{\partial f_0}{\partial v}\right)\right], \tag{11}$$

where

$$I^0_0 = n_i(\mathrm{erf}(y) - y\,\mathrm{erf}'(y)).$$

Here, erf is the standard error function and erf′ is its derivative; $y = \sqrt{m_i v^2/2kT_i}$ and $\Gamma_{ei} = (Z^2 e^4 \ln\Lambda_{ei})/(4\pi(m_e\varepsilon_0)^2)$. Conservation of energy is achieved by adding Eq. (9) to Q_e in the electron temperature equation for fluid electrons, and Eq. (11) to the right hand side of the VFPB equation for kinetic electrons.

It is worth remarking here that the assumption of Maxwellian ions for F_0 is not a particularly limiting constraint. Due to the lower thermal velocity of ions, the bulk of F_0 takes up a relatively small portion of the velocity domain compared to f_0, over which the collision operator is integrating, and so the collision operator is much more sensitive to changes in the exact shape of f_0 than F_0.

3 Simulation setup

The simulated spatial domain was 10.18m in length, where symmetry about the midplane is assumed so that this represents half of the connection length of the modelled SOL. External

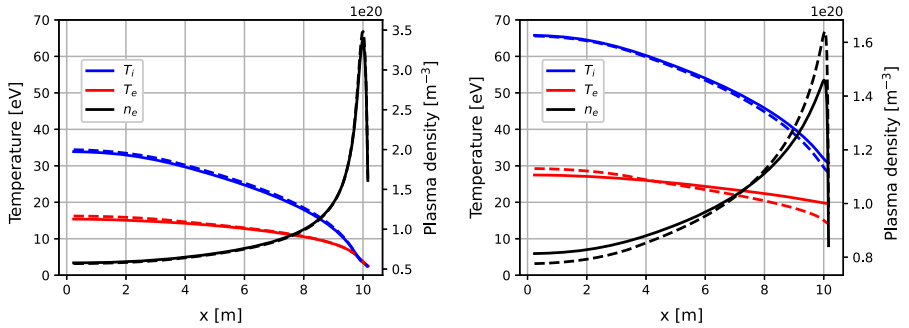

(a) Plasma conditions in equilibrium for $P_{in} = 1\text{MWm}^{-2}$. **(b)** Plasma conditions in equilibrium for $P_{in} = 6\text{MWm}^{-2}$.

Fig. 1 Plasma temperature and density profiles for a detached and non-detached case ($1\,\text{MWm}^{-2}$ and $6\,\text{MWm}^{-2}$ input power, respectively). Solid/dashed lines represent simulations with fluid/kinetic electrons. The boundary at $x = 0$ is the midplane, while $x \sim 10$m is the sheath entrance

heating is applied over the first 3.51m, simulating input power to the SOL from the core. For both fluid and kinetic electrons, equilibrium conditions were obtained for four input powers, $P_{in} = 1.0\text{MWm}^{-2}$, $3.0\,\text{MWm}^{-2}$, $4.5\,\text{MWm}^{-2}$ and $6.0\,\text{MWm}^{-2}$. Equal amounts go into the electrons and ions, so that the total input power is $2P_{in}$. In the discussion that follows, runs are referred to by the P_{in} going to each species, not the total input. The plasma response to conductive transients was also simulated, where the input power was temporarily increased to $P_{in} = 45\,\text{MWm}^{-2}$ for a duration of 10μs, before returning to the original input power.

The spatial domain was divided into 64 cells, representing the region between the midplane and the sheath entrance. Spatial cells were spaced logarithmically, with higher resolution close to the target. Spatial grid widths ranged from 0.48m to 0.03m. In velocity space (for kinetic electron runs), a geometric grid of 80 cells was used up to a velocity of $\sim 12v_{th,0}$, where $v_{th,0}$ is the thermal velocity of electrons at a reference temperature of 10eV. The resolution was higher at low velocities, such that grid widths ranged from $0.05v_{th,0}$ to $0.35v_{th,0}$.

For kinetic runs, the kinetic equation was solved up to the harmonic $l_{max} = 3$. A constant line-averaged plasma density of $\langle n \rangle = 1 \times 10^{19}\text{m}^{-3}$ was maintained through 100% recycling of neutral deuterium atoms, where thirty excited states were modelled.

The timestep used was $2t_0$ for the fluid runs and ranged from $0.01t_0$ to $0.1t_0$ for the kinetic runs depending on input power, where t_0 is the 90° electron–ion collision time for a reference plasma at $T_e = 10$eV and $n_e = 2.5 \times 10^{19}\text{m}^{-3}$.

4 Results

It is informative to first present the equilibrium plasma profiles obtained for two input powers, $P_{in} = 1\,\text{MWm}^{-2}$ and $6\,\text{MWm}^{-2}$, shown in Fig. 1. Solid lines show results for fluid electrons, while dashed lines represent simulations with kinetic electrons. In these simulations, the plasma was allowed to evolve until equilibrium was reached for the model described in Sect. 2. For the $1\,\text{MWm}^{-2}$ case, we see a detached profile; however, the $6\,\text{MWm}^{-2}$ case is not detached. The low-power run shows minimal differences when the electrons are treated kinetically, while in the high-power run (corresponding to lower collisionality) a steeper electron temperature gradient is seen (this effect is discussed in [7]). As expected, the ions tend to be hotter than the electrons, especially upstream, owing to their lower heat conductivity.

Table 1 Line-integrated ion–electron energy transfer using a kinetic or fluid model, for four different equilibrium conditions

P_{in} [MWm^{-2}]	$\langle Q_{ei}^{fl} \rangle$ [MWm^{-2}]	$\langle Q_{ei}^{kin} \rangle$ [MWm^{-2}]
1.0	0.65	0.66
3.0	1.36	1.37
4.5	1.35	1.36
6.0	1.18	1.19

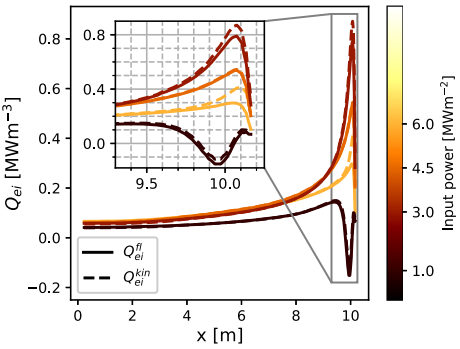

Fig. 2 Ion–electron energy exchange for kinetic equilibria at four different input powers (positive values mean energy is going to the electrons), for the electron distribution obtained by SOL-KiT, Q_{ei}^{kin} (dashed), and for a Maxwellian at the same density and temperature, Q_{ei}^{fl} (solid)

For the focus of this study, we now turn to the energy transfer between electrons and ions, Q_{ei}. We limit the analysis to the kinetic runs, exploring differences in Q_{ei} caused by deviations of the electron distribution function from Maxwellian. The reason for doing this is that the absolute value of Q_{ei} is a strong function of the temperature difference between electrons and ions, which is in turn influenced by whether a kinetic or fluid model is used for the electrons. As such, a clearer consideration of any potential kinetic effects in the heat exchange between the two species can be done by looking at plasma profiles obtained with kinetic electrons only. In Fig. 2, we compare the heat exchange calculated using Eq. (10) for the f_0 obtained by SOL-KiT, Q_{ei}^{kin}, with a Maxwellian with the same density and temperature acquired from moments of f_0, Q_{ei}^{fl} (this is effectively equivalent to using the familiar Braginskii expression in Eq. (9)). Heat exchange across most runs peaks close to the target due to reduced temperatures and increased densities leading to higher collisionality there, outcompeting the reduced temperature differences (see Fig. 1). For the lowest power run, the uptick close to the target arises because the electron and ion temperatures decouple slightly there despite high collisionality, most probably due to differences in the sheath heat transmission. Small differences can be seen between a kinetic and fluid calculation of Q_{ei}, across all runs, particularly in the high-power cases close to the target, but there is good overall agreement. In all cases, a kinetic treatment leads to a (small) suppression of energy transfer upstream, and enhanced energy transfer close to the target. Table 1 shows the total energy transfer in equilibrium integrated over the whole domain, i.e. $\langle Q_{ei} \rangle = \int Q_{ei} dx$. The differences are minimal, being less than 0.02 MWm^{-2} in all cases, suggesting Q_{ei} is well described by a fluid model here.

For the conductive transients studied, Fig. 3 shows the difference in Q_{ei} when calculated kinetically or with the fluid model, $Q_{ei}^{kin} - Q_{ei}^{fl}$, for a spatial cell in the middle of the domain ($x \simeq 5$m) and close to the target ($x \simeq 10$m). The different runs are referred to here by the

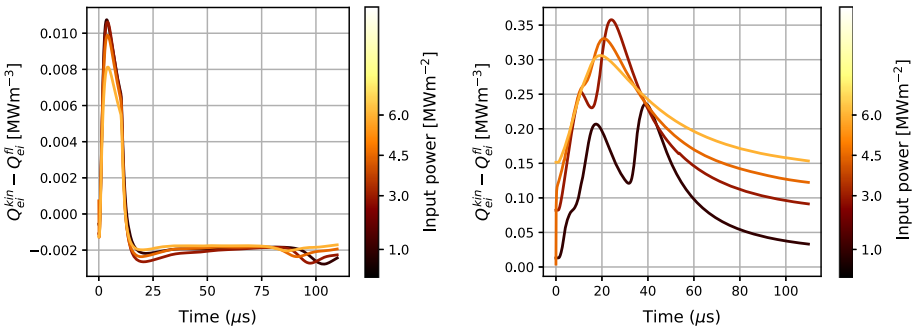

(a) $x = 5.16$m **(b)** $x = 10.14$m

Fig. 3 Time evolution of the difference in Q_{ei} for a kinetic (Q_{ei}^{kin}) and fluid (Q_{ei}^{fl}) calculation, for conductive transients launched on background equilibria obtained at four different input powers. The origin of the ripple effect occurring on an electron timescale in the lowest power runs at the target (right) is unclear, but may be connected to an oscillating detachment front

value of P_{in} prior to the transient, which represents the background plasma conditions on which the transient was launched. All runs experience the same power burst of 45 MWm^{-2} for 10μs, before returning to the original input power.

In the middle of the domain (Fig. 3a), we see enhanced energy transfer associated with the transient across all runs, before relaxing quickly to the pre-burst value (slight suppression) and a small secondary perturbation on an acoustic timescale at $t \simeq 100\mu$s. The peak occurs in all runs before the transient energy burst has finished, at around 4μs. For context, in order of increasing P_{in} the peaks in Fig. 3a represent, respectively, 44%, 18%, 14% and 11% enhancement of Q_{ei}^{kin} compared to Q_{ei}^{fl} at that time and location.

Close to the target (Fig. 3b), we see peak differences in energy exchange an order of magnitude larger than that in the middle of the domain, and slower relaxation to the pre-transient level, occurring on a timescale of the order 40-100μs. The peak kinetic enhancement of Q_{ei} happens at different times for different background plasmas, occurring 10-30μs after the transient has ended. For the 1 MWm^{-2} and 3 MWm^{-2} runs, the peak represents 25% and 63% enhancement, respectively, while for the 4.5 MWm^{-2} 6 MWm^{-2} runs, we see a doubling and tripling of the respective values of Q_{ei}^{fl}.

To assess the total magnitude of the effect seen here, we again integrate over the spatial domain and take the difference for a kinetic and fluid treatment at each point in time, $\langle Q_{ei}^{kin}\rangle - \langle Q_{ei}^{fl}\rangle$. This is shown in Fig. 4. We see that the peak kinetic enhancement of $\langle Q_{ei}\rangle$ is slightly stronger for low-power runs (corresponding to higher collisionality before the transient), and that the duration of the effect is similar to that of the transient energy burst. This is despite the fact that the area of strongest enhancement, close to the target, takes longer to relax than elsewhere—this may be explained by the fact this particularly strong effect occurs over a relatively small region. Taking the first 10μs and subsequent 40μs (up to $t = 50\mu$s), Table 2 compares the time integrated total energy transfer from the ions to the electrons during the simulations, $W_{ei} = \int \langle Q_{ei}\rangle dt$. During the transient energy burst (first 10μs), a kinetic treatment predicts 55% more energy transfer than a fluid model for the 1 MWm^{-2} background, with the effect reducing to 8% for the 6 MWm^{-2} background. There are much smaller differences in the subsequent 40μs, peaking at 3% enhancement for the 1 MWm^{-2} background, highlighting that the effect is more significant during the burst phase of the transient.

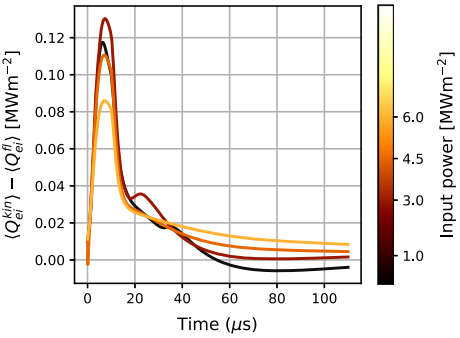

Fig. 4 Evolution during a conductive transient of the difference in Q_{ei} when calculated kinetically or with a fluid approximation, integrated over the spatial domain

Table 2 Total time-integrated ion–electron energy transfer using a kinetic or fluid model, comparing the first 10μs (duration of transient energy burst) with the following 40μs. For context, the total input energy to the plasma during the first 10μs is 900Jm^{-2}

P_{in} [MWm^{-2}]	First 10μs		Subsequent 40μs	
	W_{ei}^{fl} [Jm^{-2}]	W_{ei}^{kin} [Jm^{-2}]	W_{ei}^{fl} [Jm^{-2}]	W_{ei}^{kin} [Jm^{-2}]
1.0	1.55	2.41	32.05	33.04
3.0	8.70	9.64	51.04	52.20
4.5	9.27	10.09	41.34	42.33
6.0	8.69	9.36	34.81	35.80

5 Discussion

We have seen that ion–electron energy transfer is described well by a fluid model in the steady-state SOL regimes studied here. Differences that do exist appear unlikely to affect plasma profiles and behaviour as they are small in magnitude and occur over a relatively small region. During transient regimes, however, a kinetic treatment of the electrons predicts additional heat exchange, particularly during the transient energy burst into the SOL. Before proceeding, it is worth noting that finite grid effects are unlikely to be contributing significantly to these effects. A subset of the runs analysed here were repeated on a velocity grid with quadrupled resolution (not presented here), and only negligible differences were seen.

We may investigate the cause of the observed effects by looking at the electron distribution in a region of kinetic enhancement of Q_{ei}, and its effect on the collision operator. In Fig. 5, these quantities are shown for a spatial cell close to the target ($x = 10.16$m) at a time correlating with the peak of the enhancement in the $3\,\mathrm{MWm}^{-2}$ transient run in Fig. 3b ($t = 25\mu$s).

The obtained distribution in this region deviates strongly from a Maxwellian (Fig. 5a), featuring an additional low-temperature electron population, depletion around the middle of the energy range and an enhanced high-energy tail. This deviation contributes to the enhancement of Q_{ei}, as can be seen in Fig. 5b, where the integrand (dashed) of the energy moment of the collision operator, $Q_{ei} = \int \frac{1}{2} m v^2 C_{ei}^0 d\boldsymbol{v}$, is plotted alongside the integral (solid), as a function of electron energy. Shown are the curves for the SOL-KiT-obtained distribution and a Maxwellian, as well as that of a two-temperature Maxwellian (discussed shortly). A distinct low-energy feature can be seen, which is not present for the Maxwellian. Around the middle of the energy range, there is also some additional kinetic contribution

to Q_{ei}. The high-energy tail does not contribute to the kinetic enhancement of Q_{ei} here, as expected due to the low collisionality of fast electrons.

We might expect the additional cold electrons seen in the f_0 obtained by SOL-KiT, which produces the distinct low-energy contribution to Q_{ei} seen in Fig. 5b, to originate from electrons liberated by collisional ionization. While the exact form of this collisional operator implemented in SOL-KiT places the ejected electrons in the lowest velocity cell, and so the effect may be exaggerated, we would anyway expect electrons generated during the ionization process to be colder than the background population due to loss of the ionization energy. By fitting a two-temperature Maxwellian to the contribution to Q_{ei}, keeping overall density and temperature the same, good agreement is obtained with the low-energy feature in Fig. 5b (inset) with $T_e^{cold} = 0.13\text{eV}$ and $n_e^{cold} = 3.8 \times 10^{15}\text{m}^{-3}$. This accounts for $0.13\,\text{MWm}^{-3}$ of the additional $0.33\,\text{MWm}^{-3}$ energy exchange seen here when treated kinetically. Putting a two-temperature Maxwellian into the collision operator yields $Q_{ei} = Q_{ei}^{cold} + Q_{ei}^{bulk}$, where Q_{ei}^{cold} and Q_{ei}^{bulk} take the form of Eq. (9) with the appropriate temperature and density for the cold population and the bulk electron population, respectively. It is feasible, but not done here, that a value for the temperature and density of the cold electron population based on considerations of the ionization rate may be obtained, which could be used to modify the value of Q_{ei} used in fluid simulations.

So, the addition of a population of cold electrons arising from ionization appears to explain around a third of the enhancement in energy exchange seen here when electrons are treated kinetically. There are several factors contributing to the distortion of f_0 from Maxwellian at this location, including the presence of the sheath as well as plasma–neutral interactions and sharp temperature gradients. A simple model accounting just for ionized electrons does not fully account for the kinetic enhancement in Q_{ei} seen, and the majority component of the effect may require a kinetic model to capture accurately. It should also be noted that this effect is seen in regions where minimal ionization is occurring, albeit less strongly, as seen in Fig. 3a.

From the discussion here, it is feasible then that transient regimes may lead to increased energy coupling between electrons and ions in the divertor SOL, which would manifest as hotter electron temperatures and colder ion temperatures at the target. This would in turn impact sputtering yields and target heat flux. On the other hand, kinetic corrections to Q_{ei} on the order of 1Jm^{-2}, as seen in Table 2, contrast with a total input energy to the plasma of 900Jm^{-2} during the $10\mu\text{s}$ transient. So while a kinetic effect is apparent, even strong enhancement of Q_{ei} may not significantly affect plasma behaviour. Further investigation would therefore be required to determine the extent to which plasma profiles are modified by this effect. Given the overall, line-integrated value of the kinetic enhancement in Q_{ei} appears to only be significant during the energy burst phase of the conductive transients modelled, any impact on plasma profiles would be dependent on the frequency and duration of the transient events. For example, type I edge-localized modes (ELMs) would drive this effect differently to type III ELMs. Some saturation of the effect is observed in Fig. 4 before the energy burst has ended, raising the possibility that there is a ceiling to its magnitude, and that more energetic transients do not result in stronger kinetic enhancement of Q_{ei}. On the other hand, the effect appears to persist long after the energy burst at regions close to the target compared to elsewhere in the domain (Fig. 5b), and the saturation behaviour is not observed, so that target temperatures may be affected even if the overall energy exchange between species is modified only slightly.

It is worth remarking that the diffusive neutral model used here may lead to an underestimation of the momentum and energy transfer between the plasma and neutrals, which in

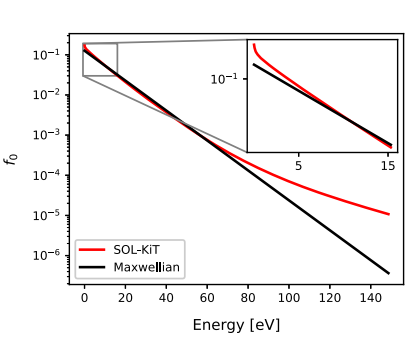

(a) f_0 obtained by SOL-KiT (red) and a Maxwellian at the same density and temperature (black). An enhanced low-temperature electron population can be seen in the SOL-KiT distribution (inset). The electron temperature at this point is 11.7eV.

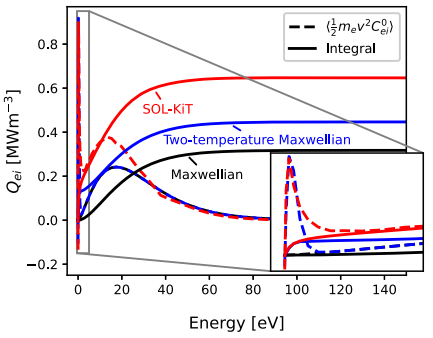

(b) The contribution to $Q_{ei} = \int \frac{1}{2}mv^2 C^0_{ei} d\boldsymbol{v}$ as a function of energy. The integrand (dashed) is shown alongside its contribution to the integral (solid). Results for the f_0 obtained by SOL-KiT (red) are shown alongside those for an equivalent Maxwellian (black) and a Maxwellian with an additional cold electron population (blue).

Fig. 5 Electron distribution function and contribution to Q_{ei} at $x = 10.16$m, during a transient on a 3 MWm^{-2} background at the peak Q_{ei} enhancement ($t \simeq 25\mu$s). The low-energy feature in the contribution to Q_{ei} (right, inset) is well approximated by a two-temperature Maxwellian, but does not explain the entire discrepancy

turn would modify plasma profiles. Work is currently ongoing to extend the neutral model in SOL-KiT, but in the regime studied here it is assumed that sources and sinks are more significant in the neutral dynamics than their momentum, for example, and refinement of the neutral behaviour is unlikely to alter the qualitative conclusions of this study.

6 Conclusion

We have presented here an extension to the SOL-KiT model, a code used for kinetic studies of parallel transport in the scrape-off layer. By allowing the electron and ion temperatures to decouple, we have then explored the consequences of this for energy transfer between the two species during equilibrium and transient conditions. It has been shown that a fluid approximation of this energy transfer shows good agreement with a kinetic treatment across a range of input powers for equilibrium conditions. Some kinetic enhancement of the energy transfer is observed during a burst of energy launched on background equilibria, reaching up to 55% for the cases considered in this study, which is not seen in a simplistic fluid model and not accounted for by a two-temperature distribution assumption. However, the magnitude of the effect is unlikely to yield strong differences in predictions of target conditions, bearing in mind that this increase represents around 0.1% the total energy going into the SOL over this time.

Given the strongly non-Maxwellian electron distributions seen in some scrape-off layer regimes (see [16], for example), it might have been expected that a fluid model would under- or overestimate the amount of energy transferred between plasma species, leading to incorrect modelling of plasma profiles and target conditions. The fact this has not been seen in this study is reassuring for fluid modelling of the scrape-off layer.

Data Availability Statement This manuscript has associated data in a data repository. [Authors' comment: All input and output data for the SOL-KiT simulations described in this paper can be found at https://doi.org/10.14469/hpc/9866.]

References

1. A. V. Chankin, D. P. Coster, G. Corrigan, S. K. Erents, W. Fundamenski, A. Kallenbach, K. Lackner, J. Neuhauser, R. Pitts, Fluid code simulations of radial electric field in the scrape-off layer of JET. Plasma Phys. Control. Fusion **51**(6)(2009)
2. B. Dudson, J. Allen, T. Body, B. Chapman, C. Lau, L. Townley, D. Moulton, J. Harrison, B. Lipschultz, The role of particle, energy and momentum losses in 1D simulations of divertor detachment. Plasma Phys. Control. Fusion **61**(6)(2019)
3. E. Havlíčková, J. Harrison, B. Lipschultz, G. Fishpool, A. Kirk, A. Thornton, M. Wischmeier, S. Elmore, S. Allan, SOLPS analysis of the MAST-U divertor with the effect of heating power and pumping on the access to detachment in the Super-x configuration. Plasma Phys. Control. Fusion **57**(11)(2015)
4. S. I. Braginskii. Transport processes in plasmas. Rev. Plasma Phys., pp. 205–311, (1965)
5. A.V. Chankin, D.P. Coster, Comparison of 2D models for the plasma edge with experimental measurements and assessment of deficiencies. J. Nuclear Mater. **390–391**(1), 319–324 (2009)
6. S. Mijin, A. Antony, F. Militello, R.J. Kingham, SOL-KiT-Fully implicit code for kinetic simulation of parallel electron transport in the tokamak Scrape-Off Layer. Comput. Phys. Commun. **258**, 107600 (2021)
7. S. Mijin, F. Militello, S. Newton, J. Omotani, R.J. Kingham, Kinetic and fluid simulations of parallel electron transport during equilibria and transients in the scrape-off layer. Plasma Phys. Control. Fusion **62**(9), 095004 (2020)
8. L. Spitzer, R. Härm, Transport phenomena in a completely ionized gas. Phys. Rev. **89**(5), 977–981 (1953)
9. R. K. Janev, D. Reiter, and U. Samm. *Collision Processes in Low-Temperature Hydrogen Plasmas*. (2003)
10. R. J. Kingham, A. R. Bell. *An implicit Vlasov-Fokker-Planck code to model non-local electron transport in 2-D with magnetic fields*, vol. 194. (2004)
11. M. Tzoufras, A.R. Bell, P.A. Norreys, F.S. Tsung, A Vlasov-Fokker-Planck code for high energy density physics. J. Comput. Phys. **230**(17), 6475–6494 (2011)
12. I. P. Shkarofsky, M. P. Bachynski, and T. W. Johnston. *The Particle Kinetics of Plasmas*. Reading, Mass.; Dordrecht printed, (1966)
13. A. Bogaerts, R. Gijbels, J. Vlcek, Collisional-radiative model for an argon glow discharge. J. Appl. Phys. **84**(1), 121–136 (1998)
14. G. Colonna, L.D. Pietanza, M. Capitelli, Coupled solution of a time-dependent collisional-radiative model and Boltzmann equation for atomic hydrogen plasmas: Possible implications with LIBS plasmas. Spectrochimica Acta Part B Atomic Spectroscopy **56**(6), 587–598 (2001)
15. A. S. Richardson. 2019 NRL plasma formulary. Plasma Phys., pp. 1–71, (2019)
16. A.A. Batishcheva, O.V. Batishchev, S.I. Krasheninnikov, D.J. Sigmar, M.M. Shoucri, I.P. Shkarofsky, Fokker-Planck simulation of electron transport in SOL plasmas with ALLA code. Contribut. Plasma Phys. **36**(2–3), 235–239 (1996)